International Journal of Solids and Structures 46 (2009) 287–310

Contents lists available at ScienceDirect

International Journal of Solids and Structures

journal homepage: www.elsevier.com/locate/ijsolstr

A new computational algorithm for contact friction modeling of large plastic deformation in powder compaction processes

A.R. Khoei *, S.O.R. Biabanaki, A.R. Vafa, I. Yadegaran, Sh. Keshavarz

Center of Excellence in Structural and Earthquake Engineering, Department of Civil Engineering, Sharif University of Technology, P.O. Box. 11365-9313, Tehran, Iran

ARTICLE INFO

Article history:
Received 12 October 2007
Received in revised form 10 August 2008
Available online 6 September 2008

Keywords:
Powder compaction
Contact friction
Node-to-surface algorithm
Cap plasticity
Large deformation

ABSTRACT

In this paper, the large deformation frictional contact of powder forming process is modeled based on a new computational algorithm by imposing the contact constraints and modifying the contact properties of frictional slip. A simple and efficient numerical algorithm is presented for imposing the contact constraints and frictional contact properties based on the node-to-surface contact technique to simulate the large deformation contact problem in the compaction process of powder. The Coulomb friction law is used to simulate the friction between the rigid punch and the workpiece by the use of penalty approach. A double-surface cap plasticity model is employed together with the nonlinear contact friction algorithm within the framework of large FE deformation in order to predict the non-uniform relative density distribution during large deformation of powder die-pressing. Finally, the numerical schemes are examined for accuracy and efficiency in modeling of a set of powder components.

1. Introduction

Contact friction is among the most difficult nonlinear problem since the response in contact interface is not smooth. In powder compaction process, the friction between the powder and tools limits the performances of the process and the mechanical characteristics of the parts. Friction can result in poor density distributions, which leads to differential retreat during compaction and sintering of the final properties of the component. Many aspects of the process are affected by friction, including: the density distribution, pressing forces, final shape, tool wear, residual stresses and cracks. In contact friction modeling, the tangential velocities along the interface are discontinues due to the stick-slip behavior between the powder and punches. These characteristics of contact introduce significant difficulties in the time integration of the discrete equations. Up to date, the most computational aspects of powder forming processes have been presented in large elasto-plasticity deformations (Khoei, 2005). However, to the knowledge of authors less numerical modeling has been reported in the description of complex phenomena along the contact surface between the powder and tools.

A number of experimental and numerical investigations into frictional effects and its impact on the compaction process of powder have been reported in the literature. Tabata et al. (1980) determined the coefficients of friction between the powder and die wall in compaction of iron powder. Ernst et al. (1991) measured the friction coefficients with the impact of lubricants on the compaction and ejection force balance. The effects of friction between the powder and the mandrel were investigated by Kim and Lee (1998) under cold isostatic pressing. They determined the friction coefficients between the powder and mandrel with different surface roughness from the relationship between the compaction pressure and the ejection pressure of the mandrel from powder compacts. Cameron and Gethin (2001) proposed a micromechanical discrete-element modeling

* Corresponding author. Tel.: +98 21 6600 5818; fax: +98 21 6601 4828.
E-mail address: arkhoei@sharif.edu (A.R. Khoei).

0020-7683/$ - see front matter © 2008 Elsevier Ltd. All rights reserved.
doi:10.1016/j.ijsolstr.2008.08.034

to investigate the friction mechanisms between the powder and tool set surfaces in die compaction. The effect of wall friction between powder-die and powder-punches was investigated by Sinka et al. (2003) in the compaction of pharmaceutical tablets, where the die and punches were lubricated and unlubricated.

The treatment of contact problem with finite element method dates back to 1970s. The early attempts were mainly towards the solution of small deformation frictionless problems (Beer, 1985). The large deformation/large sliding modeling was then performed based on the node-to-segment algorithm using the bilinear discretization of contacting bodies (Wriggers et al., 1985, 1990). The penalty and Lagrange multiplier methods were applied to enforce contact constraints (Chaudaray and Bathe, 1986; Peric and Owen, 1992). The domination of these approaches was due to their successful applications in other types of mechanics problems and their well-understood mathematical structure. Some other techniques, such as the perturbed Lagrange multiplier method and augmented Lagrange multiplier method were proposed and applied within finite element algorithms (Simo et al., 1985; Pietrzak and Curnier, 1999). In the concept of large deformation/large sliding contact problems, fundamental works were appeared by Laursen and Simo (1993,). In relation with large scale computations, the significance of contact detection algorithms was realized long ago as far as the computational time and effort is concerned (Benson and Hallquist, 1990; Belyschko and Neal, 1991). The computational algorithms have been mainly towards the contact formulation with structural elements and contact smoothing techniques in which the faceted geometry of finite element discretization is replaced by a smooth geometric approximation. Such a smooth description leads to continuous contact force distributions which would have some sharp changes with conventional finite element discretization unless a very fine mesh is used.

The contact friction is generally simulated in accordance with the Coulomb friction law, which takes into account the dependence of friction forces on contact pressure, displacement jump and material properties of contact surface (Wriggers et al., 1990). From the numerical point of view, the most important work related with the Coulomb friction law was presented by Curnier and Alart (1988), where the analogy between plasticity and frictional constitutive laws was recognized. Within the numerical context, the efforts of Giannakopoulos (1989) indicated the applicability of integration schemes used in plasticity theory to the laws describing friction phenomena.

The objective of present study is focused on a computational algorithm for simulation of large deformation contact problem based on the node-to-surface contact algorithm in the compaction process of powder. The plan of the paper is as follows; in Section 2, a general formulation of continuum model is presented for large FE deformation based on the Lagrangian description. Section 3 is devoted to the frictional contact formulation and its computational algorithm for analyzing the phenomena. The implementation of penalty approach into the node-to-surface contact modeling together with the plasticity theory of friction are demonstrated in this section. In Section 4, the double-surface cap plasticity is presented for description of powder behavior. In Section 5, numerical simulation of several complicated die geometries are presented. Finally, some concluding remarks are given in Section 6.

2. Large deformation finite element

In nonlinear elasto-plastic analyses, whether the displacements, or strains, are large or small it is imperative that the equilibrium conditions between the internal and external forces are satisfied. The equilibrium equation of a body can be therefore written in a standard form as

$$\frac{\partial P_{ji}}{\partial X_j} + b_i = 0, \tag{1}$$

where X_j is the Lagrangian coordinate, b_i is the body force and P_{ji} is the nominal stress. The above differential equation is written in the reference configuration, which is the initial configuration for the Lagrangian description. A general description of strains was introduced by Green and St. Venant, in which the non-linear strain displacement relationship can be defined in terms of the infinitesimal and large displacement components, i.e. $\boldsymbol{E} = \boldsymbol{E}_{\mathrm{L}} + \boldsymbol{E}_{\mathrm{NL}}$, with $\boldsymbol{E}_{\mathrm{L}}$ and $\boldsymbol{E}_{\mathrm{NL}}$ denoting the linear and nonlinear strains. In small displacement theory, the general first-order linear strain approximation is obtained by neglecting the quadratic terms. In this relation, the nonlinear terms of strain $\boldsymbol{E}_{\mathrm{NL}}$ can be defined by $\boldsymbol{E}_{NL} = (1/2)A_\theta\boldsymbol{\theta}$, with $\boldsymbol{\theta}$ denoting the displacement gradient and $\boldsymbol{A}_\theta$ a suitably defined matrix operator which contains displacement derivatives.

In order to develop a finite element formulation, we need to solve Eq. (1) numerically for spatial discretization. Following the standard procedure of the finite element method, the initial domain Ω is divided into elements. If the displacements within an element are prescribed in the usual manner by a finite number of nodal values, we can obtain the equilibrium equations using the virtual work principle. Thus, Eq. (1) can be written in the weak form as

$$\int_\Omega \delta\mathbf{F}^{\mathrm{T}}\mathbf{P}\,\mathrm{d}\Omega - \int_\Omega \delta\mathbf{u}^{\mathrm{T}}\mathbf{b}\,\mathrm{d}\Omega - \int_{\Gamma_{\mathrm{t}}} \delta\mathbf{u}^{\mathrm{T}}\bar{\mathbf{t}}\,\mathrm{d}\Gamma = 0, \tag{2}$$

where $\delta F_{ij} = \partial(\delta u_i)/\partial X_j = \partial x_i/\partial X_j$ is the deformation gradient. Applying the standard finite element Galerkin discretization process to Eq. (2) with the independent approximations of $\mathbf{u}$ defined as $\mathbf{u} = \mathbf{N}^{\mathrm{T}}\bar{\mathbf{u}}$, we will arrive at

$$\boldsymbol{\Psi}(\bar{\mathbf{u}}) = \int_\Omega \mathbf{B}^{\mathrm{T}}\mathbf{P}\,\mathrm{d}\Omega - \mathbf{f} = 0, \tag{3}$$

where $\mathbf{B}$ is the matrix of Cartesian shape function derivatives, defined by $B_{jI} = \partial N_I/\partial X_j$ and $\mathbf{f}$ is the load vector. There is of little interest to write the nodal forces in terms of the nominal stress $\mathbf{P}$ since this type of stress is not symmetric. Therefore, we will write Eq. (3) in terms of the second Piola–kirchhoff (PK2) stress $\mathbf{S}$, in which $\mathbf{P} = \mathbf{FS}$. Substituting this transformation into expression (3), it can be then rewritten as

$$\boldsymbol{\Psi}(\bar{\mathbf{u}}) = \int_{\Omega} \overline{\mathbf{B}}^{\mathrm{T}}\mathbf{S}\,\mathrm{d}\Omega - \mathbf{f} = 0, \tag{4}$$

where the matrix $\overline{\mathbf{B}}$ is defined based on $\mathbf{B}$ and the deformation gradient $\mathbf{F}$, as $\overline{\mathbf{B}} = \mathbf{F}^{\mathrm{T}}\mathbf{B}$, in which the matrix $\overline{\mathbf{B}}$ can be defined in terms of the matrix operator of displacement derivatives $\boldsymbol{A}_\theta$ and the matrix of Cartesian shape function derivatives $\mathbf{G}$, i.e. $\overline{\mathbf{B}}_I = \mathrm{d}\boldsymbol{A}_\theta\mathbf{G}_I$.

In order to obtain the tangential stiffness matrix, the finite element Galerkin discretization formulation (4) is appropriately taken variations with respect to $\mathrm{d}\bar{\mathbf{u}}$. In this case, the only variable that depends on the displacement is the nominal stress, thus

$$\mathrm{d}\boldsymbol{\Psi} = \int_{\Omega} \mathbf{B}^{\mathrm{T}}\,\mathrm{d}\mathbf{P}\,\mathrm{d}\Omega \equiv \overline{\mathbf{K}}_{\mathrm{T}}\,\mathrm{d}\bar{\mathbf{u}}. \tag{5}$$

For a set of virtual displacements, the corresponding $\mathrm{d}\mathbf{P}$ in Eq. (5) can be obtained by taking the derivative of transformation $\mathbf{P} = \mathbf{FS}$, i.e. $\mathrm{d}\mathbf{P} = \mathbf{F}\,\mathrm{d}\mathbf{S} + \mathrm{d}\mathbf{F}\ \mathbf{S}$. Substituting $\mathrm{d}\mathbf{P}$ into relation (5) yields to

$$\mathrm{d}\boldsymbol{\Psi} = \int_{\Omega} \mathbf{B}^{\mathrm{T}}\mathbf{F}\,\mathrm{d}\mathbf{S}\,\mathrm{d}\Omega + \int_{\Omega} \mathbf{B}^{\mathrm{T}}\,\mathrm{d}\mathbf{F}\mathbf{S}\,\mathrm{d}\Omega \equiv \mathrm{d}\boldsymbol{\Psi}^{\mathrm{mat}} + \mathrm{d}\boldsymbol{\Psi}^{\mathrm{geo}}. \tag{6}$$

The above equation shows that the stiffness matrix $\overline{\mathbf{K}}_{\mathrm{T}}$ consists of two parts: the first part involves the derivative of stress $\mathrm{d}\mathbf{S}$, which depends on the material response and leads to the material tangent stiffness matrix $\mathbf{K}^{\mathrm{mat}}$, and the second part involves the current state of stress $\mathbf{S}$, which accounts for the geometric effects of the deformation (including rotation and stretching) and leads to the geometric stiffness matrix $\mathbf{K}^{\mathrm{geo}}$ (Khoei, 2005; Khoei et al., 2006).

In order to derive the material tangent stiffness matrix $\mathbf{K}^{\mathrm{mat}}$ in Eq. (6), implement the constitutive law definition with respect to the incremental PK2 stress, i.e. $\mathrm{d}\mathbf{S} = \mathbf{D}_S^{\mathrm{ep}}\,\mathrm{d}\boldsymbol{E}$, into Eq. (6), we will have

$$\mathrm{d}\boldsymbol{\Psi}^{\mathrm{mat}} = \int_{\Omega} \mathbf{B}^{\mathrm{T}}\mathbf{F}\mathbf{D}_{\mathbf{S}}^{\mathrm{ep}}\,\mathrm{d}\boldsymbol{E}\,\mathrm{d}\Omega \equiv \mathbf{K}^{\mathrm{mat}}\,\mathrm{d}\bar{\mathbf{u}}, \tag{7}$$

where the incremental Green's strain $\mathrm{d}\boldsymbol{E}$ is defined as $\mathrm{d}\boldsymbol{E} = \overline{\mathbf{B}}\,\mathrm{d}\bar{\mathbf{u}}$. Substituting $\overline{\mathbf{B}} = \mathbf{F}^{\mathrm{T}}\mathbf{B}$ in above relation yields to

$$\mathbf{K}^{\mathrm{mat}} = \int_{\Omega} \overline{\mathbf{B}}^{\mathrm{T}}\mathbf{D}_{\mathbf{S}}^{\mathrm{ep}}\overline{\mathbf{B}}\,\mathrm{d}\Omega. \tag{8}$$

In order to derive the geometric stiffness matrix $\mathbf{K}^{\mathrm{geo}}$ in Eq. (6), implement the relation $\mathrm{d}\mathbf{F} = \mathbf{B}\,\mathrm{d}\bar{\mathbf{u}}$ into the geometric term $\mathrm{d}\boldsymbol{\Psi}^{\mathrm{geo}}$, results

$$\mathrm{d}\boldsymbol{\Psi}^{\mathrm{geo}} = \int_{\Omega} \mathbf{G}^{\mathrm{T}}\mathbf{M}_{\mathbf{S}}\mathbf{G}\,\mathrm{d}\bar{\mathbf{u}}\,\mathrm{d}\Omega \equiv \mathbf{K}^{\mathrm{geo}}\,\mathrm{d}\bar{\mathbf{u}}, \tag{9}$$

where $\mathbf{M}_{\mathbf{S}}$ is a 4×4 matrix of the three PK2 stress components for plain stress/strain problems and is defined by

$$\mathbf{M}_{\mathbf{S}} = \begin{bmatrix} S_{xx}\mathbf{I}_{2\times 2} & S_{xy}\mathbf{I}_{2\times 2} \\ S_{yx}\mathbf{I}_{2\times 2} & S_{yy}\mathbf{I}_{2\times 2} \end{bmatrix}, \tag{10}$$

where $\mathbf{I}$ is the identity matrix. Thus, we can define the total tangential stiffness matrix $\overline{\mathbf{K}}_{\mathrm{T}}$, used in Eq. (5), as

$$\overline{\mathbf{K}}_{\mathrm{T}} = \mathbf{K}^{\mathrm{mat}} + \mathbf{K}^{\mathrm{geo}} = \int_{\Omega} \overline{\mathbf{B}}^{\mathrm{T}}\mathbf{D}_{\mathbf{S}}^{\mathrm{ep}}\overline{\mathbf{B}}\,\mathrm{d}\Omega + \int_{\Omega} \mathbf{G}^{\mathrm{T}}\mathbf{M}_{\mathbf{S}}\mathbf{G}\,\mathrm{d}\Omega. \tag{11}$$

All the ingredients necessary for computing large deformation problems are now available. For each iterations, $(\overline{\mathbf{K}}_{\mathrm{T}})_{\mathrm{n}}$ is obtained from Eq. (11). The Cauchy stress $\boldsymbol{\sigma}$ is calculated based on PK2 stress using $\boldsymbol{\sigma} = J^{-1}\mathbf{FSF}^{\mathrm{T}}$, with J denoting the determinant of $\mathbf{F}$, i.e. $J = \det(\mathbf{F})$.

3. Contact friction modeling

Compared to regular initial boundary value problems, special boundary constraints are imposed in contact problems which govern the interface motion and possible singularities. For classical contact problems the constraints express non-penetration (unilateral) condition, third Newton's law and law of surface friction. The normal contact condition prevents the penetration of one body into another and the tangential slip represents frictional behavior of a contact surface. There are various approaches established for resolving the contact problem. One of these techniques applied for imposing contact conditions in the normal direction is the formulation of non-penetration condition, as a purely geometrical constraint. For the tangential direction, the sticking and sliding states can be distinguished by the development of elastic-plastic constitutive laws. In sticking interfaces, either a geometrical constraint equation, or a constitutive law for the tangential relative

micro displacements between the contacting bodies can be applied. For tangential sliding between bodies, a special constitutive equation for friction must be employed. In this study, a simple and efficient algorithm is employed to model the frictional contact in powder-die interface. The contact constraints is implemented based on the penalty approach by imposing the normal and tangential springs at the contact interface, in which the stiffness of tangential spring is modified according to the Coulomb friction law for the frictional slip.

3.1. Modeling of contact constraints

The node-to-segment (NTS) contact element is one of the most commonly used discretizations in large deformation finite element simulation of contact problems. Consider that the discrete slave point s with coordinate $\mathbf{x}^s$ comes into contact with the master segment (1)–(2) defined by the nodal coordinates $\mathbf{x}_1^{\mathrm{m}}$ and $\mathbf{x}_2^{\mathrm{m}}$. By introducing the surface coordinate ξ along the master surface, we have

$$\hat{\mathbf{x}}^{\mathrm{m}}(\xi) = \mathbf{x}_1^{\mathrm{m}} + (\mathbf{x}_2^{\mathrm{m}} - \mathbf{x}_1^{\mathrm{m}})\xi. \tag{12}$$

The normalized tangent vector of the master segment can be easily computed as

$$\mathbf{t}_{\mathrm{m}} = \frac{1}{l}\hat{\mathbf{x}}^{\mathrm{m}}(\xi)_{,\xi} = \frac{1}{l}(\mathbf{x}_2^{\mathrm{m}} - \mathbf{x}_1^{\mathrm{m}}), \tag{13}$$

where $l = \|\mathbf{x}_2^{\mathrm{m}} - \mathbf{x}_1^{\mathrm{m}}\|$. The unit normal to the segment (1)–(2) can be then computed by

$$\mathbf{n}_{\mathrm{m}} = \mathbf{e}_3 \times \mathbf{t}_{\mathrm{m}}. \tag{14}$$

The minimal distance can be then obtained as

$$g_N = [\mathbf{x}^s - (1-\bar{\xi})\mathbf{x}_1^{\mathrm{m}} - \bar{\xi}\mathbf{x}_2^{\mathrm{m}}] \cdot \mathbf{n}_{\mathrm{m}} \tag{15}$$

In order to perform the contribution of NTS element into the weak form of equilibrium equation, a new approach is applied by introducing the contact constraints based on the potential energy of springs imposed at the normal and tangential directions. In this technique, two springs are defined in the normal and tangential directions of contact interface between the slave node and master segment. The shape functions of the slave–master at the contact interface are defined as

$$\mathbf{N} = \begin{bmatrix} 1 & 0 & -(1-\xi) & 0 & -\xi & 0 \\ 0 & 1 & 0 & -(1-\xi) & 0 & -\xi \end{bmatrix}. \tag{16}$$

The relative displacement between the slave and master is defined by $\mathbf{N}\,\mathrm{d}\bar{\mathbf{u}}$, with $\mathrm{d}\bar{\mathbf{u}}$ denoting the nodal displacements. The normal and tangential relative displacements are derived using the normal and tangential shape functions as

$$\begin{aligned} \mathbf{N}_{\mathrm{n}} &= (\mathbf{n}_{\mathrm{m}} \otimes \mathbf{n}_{\mathrm{m}})\mathbf{N}, \\ \mathbf{N}_{\mathrm{t}} &= (\mathbf{I} - \mathbf{n}_{\mathrm{m}} \otimes \mathbf{n}_{\mathrm{m}})\mathbf{N}, \end{aligned} \tag{17}$$

in which the normal and tangential relative displacements are defined by $\mathrm{d}u_{\mathrm{n}} = \mathbf{n}_{\mathrm{m}}^{\mathrm{T}}\mathbf{N}_{\mathrm{n}}\,\mathrm{d}\bar{\mathbf{u}}$ and $\mathrm{d}u_{\mathrm{t}} = \mathbf{t}_{\mathrm{m}}^{\mathrm{T}}\mathbf{N}_{\mathrm{t}}\,\mathrm{d}\bar{\mathbf{u}}$, respectively.

In order to incorporate the contact constraints into the equilibrium equation, the potential energy of contact interface is decomposed into the normal and tangential directions as

$$\Pi = \frac{1}{2}\alpha_{\mathrm{n}}(\mathrm{d}u_{\mathrm{n}})^2 + \frac{1}{2}\alpha_{\mathrm{t}}(\mathrm{d}u_{\mathrm{t}})^2 = \frac{1}{2}(\mathrm{d}\mathbf{u})^{\mathrm{T}}\mathbf{N}_{\mathrm{n}}^{\mathrm{T}}\alpha_{\mathrm{n}}\mathbf{N}_{\mathrm{n}}(\mathrm{d}\mathbf{u}) + \frac{1}{2}(\mathrm{d}\mathbf{u})^{\mathrm{T}}\mathbf{N}_{\mathrm{t}}^{\mathrm{T}}\alpha_{\mathrm{t}}\mathbf{N}_{\mathrm{t}}(\mathrm{d}\mathbf{u}), \tag{18}$$

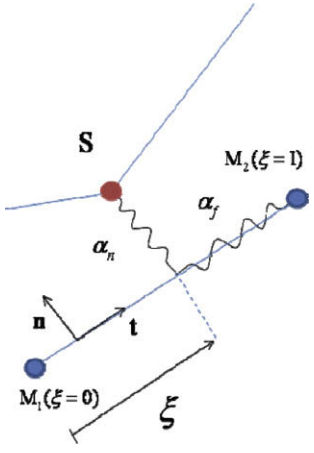

Fig. 1. Modeling of contact constraints in normal and tangential directions.

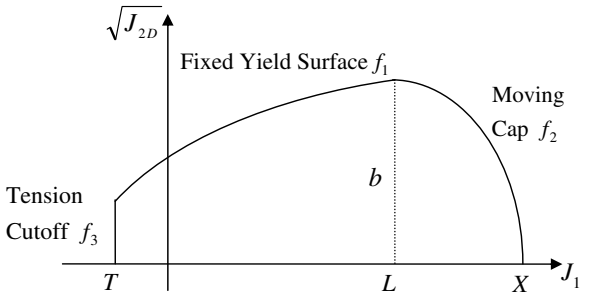

Fig. 2. The double-surface cap plasticity model.

where α_n and α_t are the normal and tangential penalty parameters, as shown in Fig. 1. Taking the derivative from relation (18), the normal and tangential stiffness matrices at the contact interface are defined as

$$\begin{aligned}\mathbf{K}_n^c &= \mathbf{N}_n^T \alpha_n \mathbf{N}_n,\\ \mathbf{K}_t^c &= \mathbf{N}_t^T \alpha_t \mathbf{N}_t.\end{aligned} \tag{19}$$

3.2. Contact friction algorithm

In order to implement the contact constraint of frictional slip, the Coulomb friction law is incorporated in the tangential spring. According to the numerical procedure described in preceding sections, a computational algorithm is applied based on the Newton–Raphson technique. For iteration i within the time step n, the following algorithm is performed:

i. Read the incremental displacement of the nodal points.
ii. Set the position of 'slave node' – 'master segment' point.
iii. Search those 'slave nodes' that are in contact with the 'master segment', and determine the values of displacement at the current time step.
iv. Evaluate the stiffness matrices $(\mathbf{K}_n^c, \mathbf{K}_t^c)$ using appropriate α_f, and assemble into a global stiffness matrix (at the first iteration of each time step, set $\alpha_f = \alpha_t$, for subsequent iterations, α_f is calculated from step 'ix' and α_n is taken as a constant value).
v. Solve the global system of equilibrium equation $\mathbf{K}_{tot}^i \delta\bar{\mathbf{u}}^i = \delta\mathbf{f}^i$.
vi. Compute the incremental nodal displacement at the next iteration $\Delta\bar{\mathbf{u}}^i = \Delta\bar{\mathbf{u}}^{i-1} + \delta\bar{\mathbf{u}}^i$, $\delta\bar{\mathbf{u}}^0 = 0$.

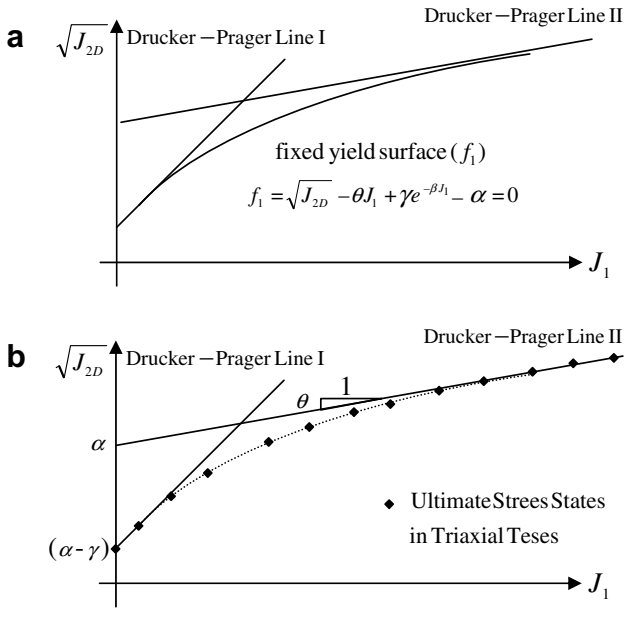

Fig. 3. The fixed yield surface of double-surface plasticity: (a) the model description and (b) the parameter determination.

vii. Determine the normal and tangential forces at each slave-master point, in order to modify the value of tangential force

$$\Delta F_{\mathrm{t}} = \alpha_{\mathrm{t}} \mathbf{t}_{\mathrm{m}}^{\mathrm{T}} \mathbf{N}_{\mathrm{t}} \Delta \bar{\mathbf{u}}^{i},$$
$$\Delta F_{\mathrm{n}} = \alpha_{\mathrm{n}} \mathbf{n}_{\mathrm{m}}^{\mathrm{T}} \mathbf{N}_{\mathrm{n}} \Delta \bar{\mathbf{u}}^{i}. \tag{20}$$

viii. Compute the maximum frictional force based on the Coulomb friction law as

$$(\Delta F_{\mathrm{t}})_{\max} = C_{\mathrm{f}} - \mu_{\mathrm{f}} (\Delta F_{\mathrm{n}}), \tag{21}$$

where C_{f} and μ_{f} are the cohesion and friction coefficient of contact interface.

ix. Correct the values of ΔF_{t} and α_{f} if $\Delta F_{\mathrm{t}} > (\Delta F_{\mathrm{t}})_{\max}$, according to

$$\alpha_{\mathrm{f}} = \left| \frac{(\Delta F_{\mathrm{t}})_{\max}}{\Delta u_{\mathrm{t}}} \right| \quad \text{and} \quad \Delta F_{\mathrm{t}} = (\Delta F_{\mathrm{t}})_{\max} \frac{\Delta u_{\mathrm{t}}}{|\Delta u_{\mathrm{t}}|}. \tag{22}$$

x. Evaluate the out of balance force, or residual force, of contact constraints:

$$\mathbf{R}_{\mathrm{n}} = \mathbf{N}_{\mathrm{n}}^{\mathrm{T}} \alpha_{\mathrm{n}} \mathbf{N}_{\mathrm{n}} \Delta \bar{\mathbf{u}},$$
$$\mathbf{R}_{\mathrm{t}} = \Delta F_{\mathrm{t}} \mathbf{t}_{\mathrm{m}}^{\mathrm{T}} \mathbf{N}_{\mathrm{t}} \Delta \bar{\mathbf{u}}. \tag{23}$$

Computational algorithm (i)–(x) are repeated until the norm of residual forces and maximum residual are both less than prescribed tolerance.

4. Powder constitutive model

During compaction, powders exhibit strain or work hardening, the volume reduces and the material becomes harder. In this case, an appropriate constitutive model needs to describe the nonlinear behavior of powders. A number of constitutive models for the cold compaction of metal powders have been proposed during last three decades, including: micromechanical models (Fleck, 1995; Ransing et al., 2000) and macromechanical models (Brekelmans et al., 1991; Haggblad and Oldenburg, 1994; Aydin et al., 1996; Khoei and Lewis, 1998, 1999; Khoei et al. 2003–2005). The cone-cap model based on a density-dependent Drucker–Prager yield surface and a non-centered ellipse is developed by Brandt and Nilsson (1999), Gu et al. (2001) and Lewis and Khoei (2001). In the present study, a double-surface cap plasticity model, based on a combination of a convex yield surface consisting of a failure envelope and a hardening elliptical

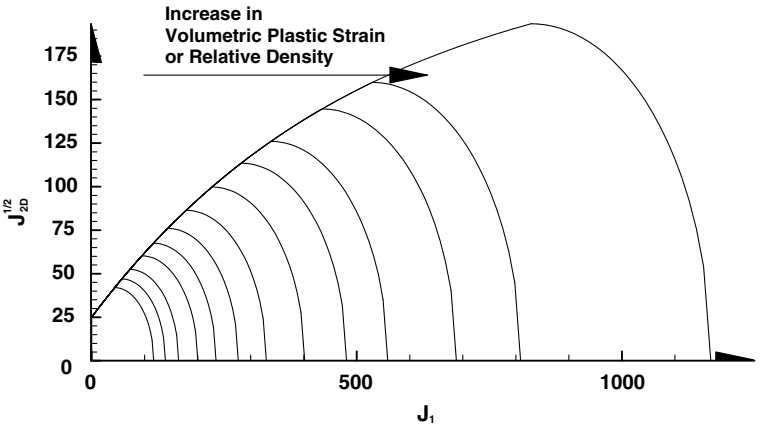

Fig. 4. The expansion of moving cap surface with increasing the volumetric plastic strain, or relative density.

Table 1
The material model parameters for the cap plasticity

Fixed surface parameters	Cap parameters	Tension cutoff
α = 225 MPa	R = 1.75	T = −0.3 MPa
β = 0.002 MPa^{-1}	D = 0.005 MPa	
γ = 200 MPa	W = 0.34	
θ = 0.008	X_0 = 1 MPa	

cap is proposed for the nonlinear behavior of powder materials. The model reflects the yielding, frictional and densification characteristics of powder along with strain and geometrical hardening which occur during the compaction process.

In order to describe the powder behavior during the compaction process, an appropriate constitutive model is employed based on the double-surface plasticity, as shown in Fig. 2. The model is based on the concept of continuous yielding of powders, expressed in terms of a three-dimensional state of stress and formulated on the basis of consistent mechanics principles. The yield surface of this elasto-plastic model has a moving cap, intersecting the hydrostatic loading line, whose position is a function of plastic volumetric strain. The main features of the cap model include a failure surface and an elliptical yield cap which closes the open space between the failure surface and the hydrostatic axis. The cap surface expands in the stress space according to a specified hardening rule. The functional forms for these surfaces are

$$f_1 = \sqrt{J_{2D}} - \theta J_1 + \gamma e^{-\beta J_1} - \alpha = 0, \tag{24}$$

$$f_2 = R^2 J_{2D} + (J_1 - L)^2 - R^2 b^2 = 0, \tag{25}$$

$$f_3 = J_1 - T = 0, \tag{26}$$

where J_1 and J_{2D} are the first invariant of stress tensor and second invariant of deviatoric stress tensor, respectively. α, β, γ and θ are the parameters of fixed yield surface f_1, which controls the deviatoric stress limits. The fixed yield surface f_1 is

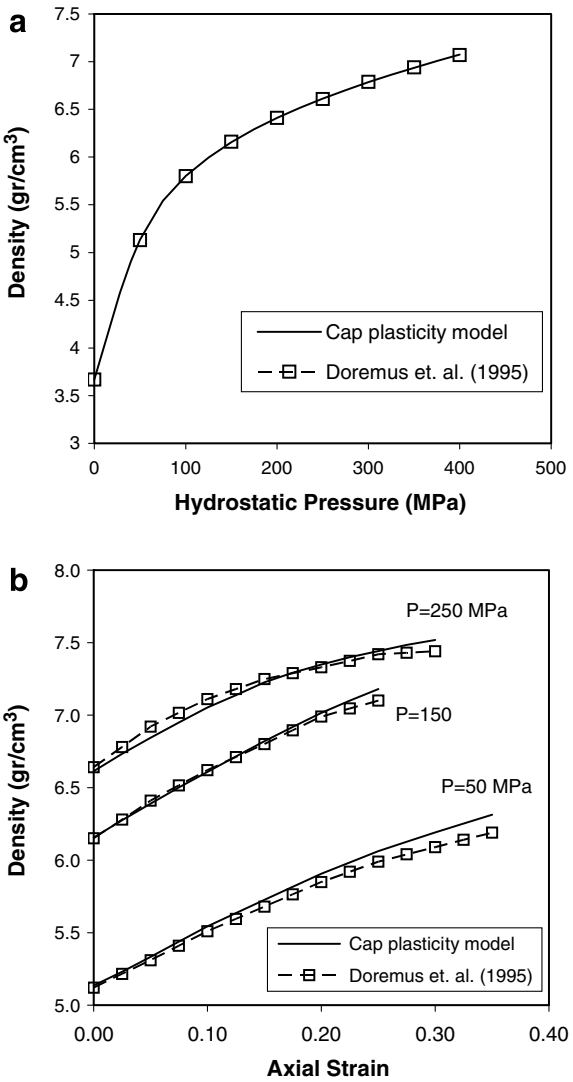

Fig. 5. A comparison of numerical and experimental results in confining pressure and triaxial tests: (a) the density versus hydrostatic pressure and (b) the density versus axial strain.

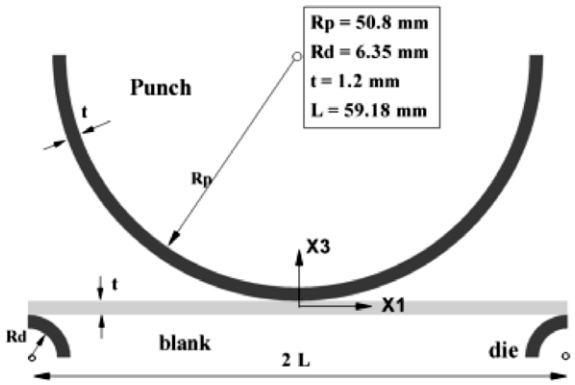

Fig. 6. Plane strain stretching of a thin sheet by a cylindrical punch: the geometry and boundary conditions.

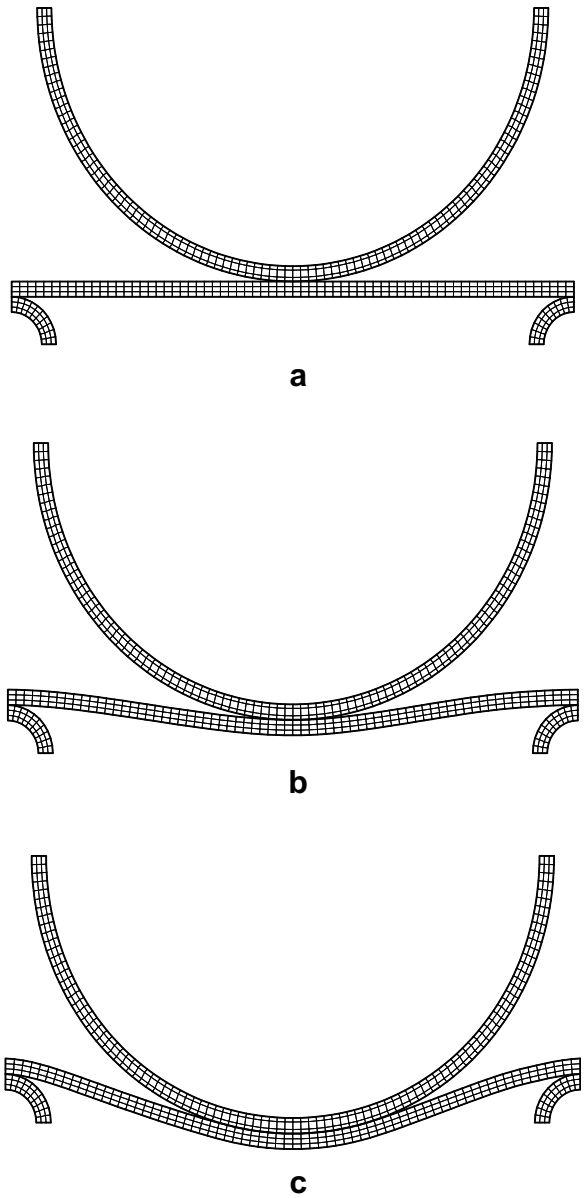

Fig. 7. Finite element modeling of a thin sheet by a cylindrical punch: (a) initial configuration, (b) deformed mesh at 50% and (c) deformed mesh at 100%.

defined by an exponential function and in reality is consist of two different Drucker–Prager yield surfaces. The cap yield surface f_2 is an elliptical function, with R denoting the ratio of two elliptical cap's diameters. The function f_3 indicates the tension cutoff zone, with T denoting the material's tension limit.

The hardening rule for moving cap is related to the volumetric plastic strain ε_v^p as

$$X(\kappa) = X(\varepsilon_v^p) = \frac{-1}{D} \ln\left(\frac{1-\varepsilon_v^p}{W}\right) + X_0, \tag{27}$$

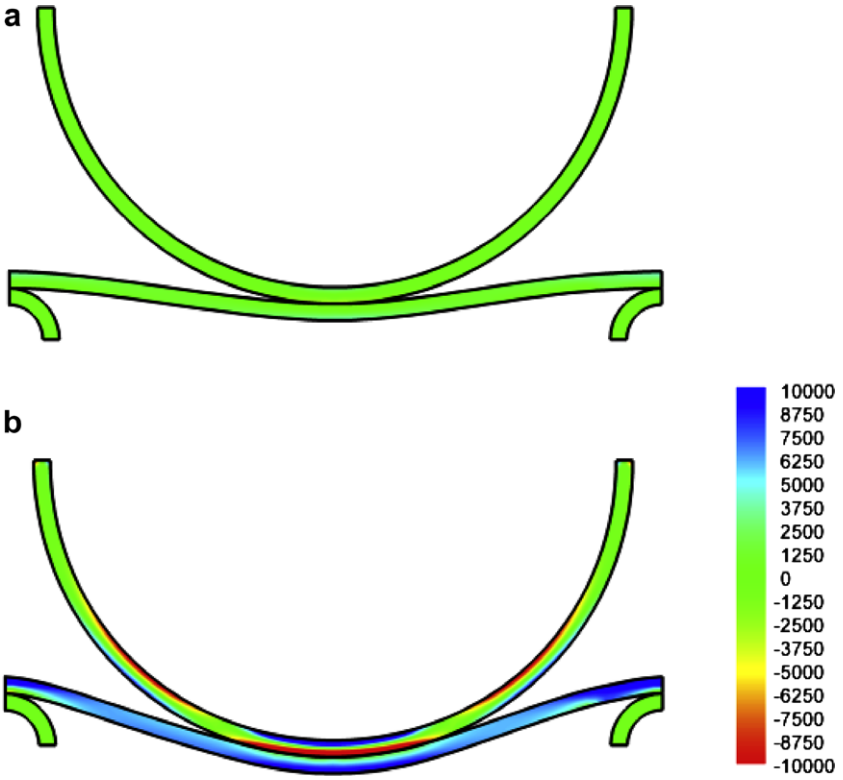

Fig. 8. Stress distribution contours of a thin sheet by a cylindrical punch at: (a) 50% and (b) 100%.

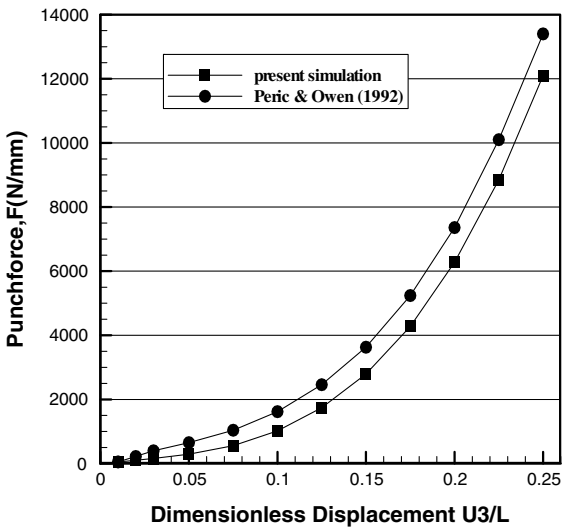

Fig. 9. Plain strain stretching of a thin sheet by a cylindrical punch: the variation of top punch reaction with vertical displacement.

where D and W are material parameters and X_0 refers to the position of initial cap surface. The plastic hardening/softening modulus H is zero for f_1 and f_3.

4.1. Material property matrix

In order to compute the powder elasto-plastic constitutive matrix, we need to calculate the plastic hardening/softening modulus and flow direction vector in the matrix $\mathbf{D}^{ep}$, defined by

$$\mathbf{D}^{ep} = \mathbf{D}^{e} - \frac{\mathbf{D}^{e}\mathbf{n}_Q\mathbf{n}_F^{T}\mathbf{D}^{e}}{H + \mathbf{n}_F^{T}\mathbf{D}^{e}\mathbf{n}_Q} \tag{28}$$

where $\mathbf{D}^{e}$ is the elastic constitutive matrix ($d\boldsymbol{\sigma}^{e} = \mathbf{D}^{e}\, d\varepsilon$), H is the plastic hardening/softening modulus, $\mathbf{n}_F$ is the normal vector to yield surface ($\partial F/\partial\boldsymbol{\sigma}$) and $\mathbf{n}_Q$ is the normal vector to plastic potential surface ($\partial Q/\partial\boldsymbol{\sigma}$). The plastic hardening/softening modulus and flow direction vector are defined as

$$H = -\left(\frac{\partial F}{\partial \kappa}\right)\left(\frac{\partial \kappa}{\partial \boldsymbol{\varepsilon}}\right)^{T}\mathbf{n}_Q, \tag{29}$$

$$\frac{\partial F}{\partial \boldsymbol{\sigma}} = C_1\frac{\partial J_1}{\partial \boldsymbol{\sigma}} + C_2\frac{\partial (J_{2D})^{1/2}}{\partial \boldsymbol{\sigma}} + C_3\frac{\partial J_{3D}}{\partial \boldsymbol{\sigma}}, \tag{30}$$

where $C_1 = \partial F/\partial J_1$, $C_2 = \partial F/\partial (J_{2D})^{1/2}$ and $C_3 = \partial F/\partial J_{3D}$.

For the fixed yield surface, the values of constants C_1, C_2 and C_3 in the case of associated flow rule are as follows: $C_1 = -\theta - \beta\gamma e^{-\beta J_1}$, $C_2 = 1$ and $C_3 = 0$. Considering function f_2 in Eq. (25) the values of constants C_i for moving cap surface are defined as: $C_1 = (1/Rb)(J_1 - L)$, $C_2 = (1/b)R\sqrt{J_{2D}}$ and $C_3 = 0$. Finally, the values of constants C_1, C_2 and C_3 for the tension cut-off yield surface can be simply calculated according to Eq. (26) as $C_1 = -1.0$, $C_2 = 0$ and $C_3 = 0$. The plastic hardening/softening modulus for the fixed yield surface and tension cut-off surface is assumed to be zero. For moving cap surface, the plastic modulus H can be obtained by substituting f_2 from Eq. (25) into relation (29) as

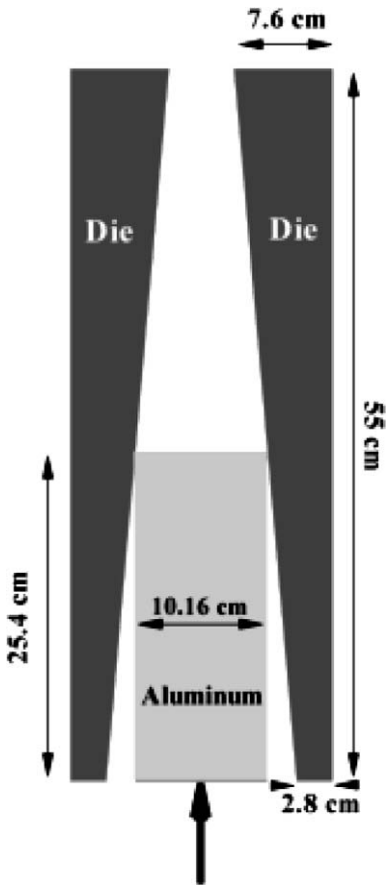

Fig. 10. The extrusion of an aluminum billet: the geometry and boundary conditions.

$$H = -\left(\frac{\partial f_2}{\partial \varepsilon_v^p}\right)\left(\frac{\partial \varepsilon_v^p}{\partial \varepsilon}\right)^T \mathbf{n}_Q = -\left(\frac{\partial f_2}{\partial \varepsilon_v^p}\right)(n_{Qii}), \tag{31}$$

where

$$\frac{\partial f_2}{\partial \varepsilon_v^p} = \frac{\partial f_2}{\partial L}\frac{\partial L}{\partial \varepsilon_v^p} + \frac{\partial f_2}{\partial b}\frac{\partial b}{\partial \varepsilon_v^p}, \tag{32}$$

where $\partial f_2/\partial L = 2(J_1 - L)$, $\partial f_2/\partial b = -2R^2 b$ and

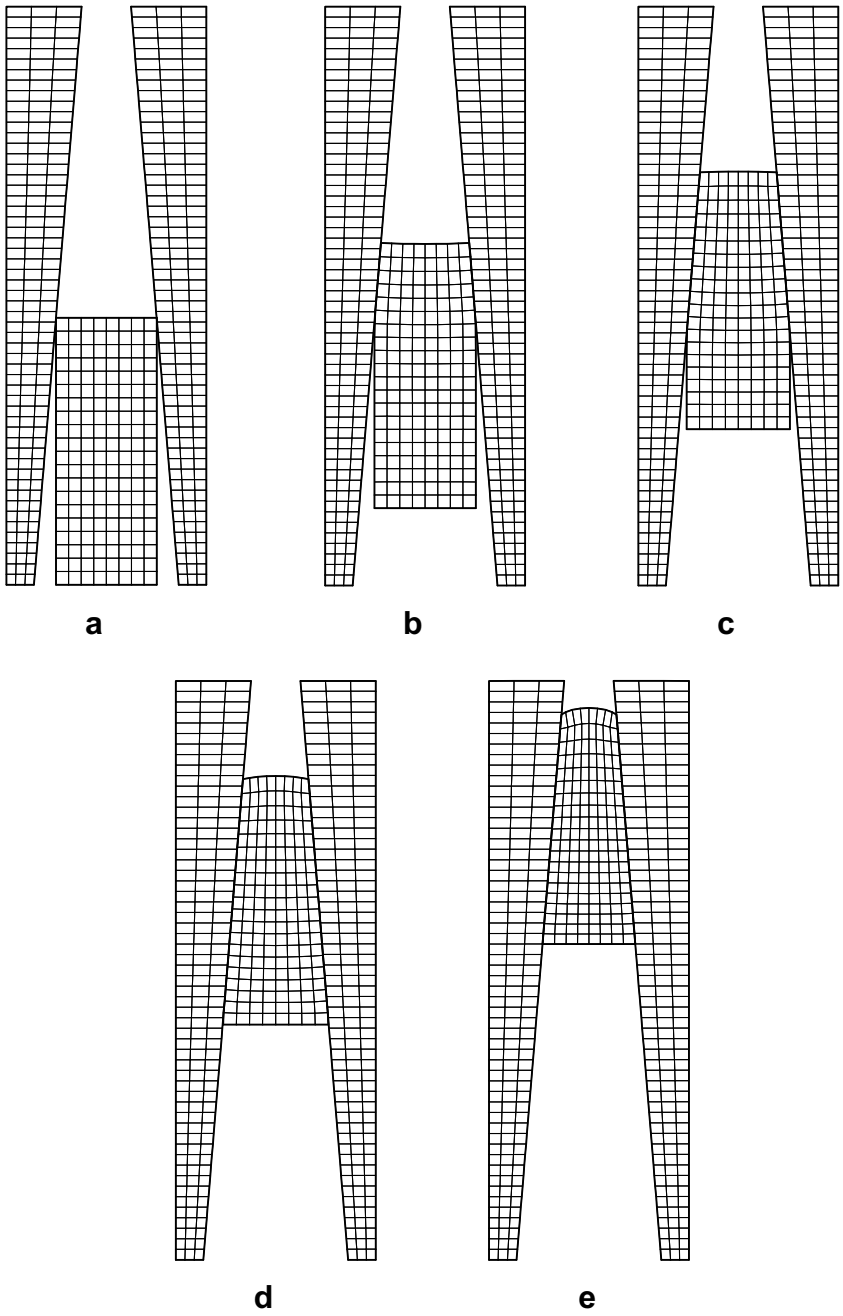

Fig. 11. Finite element modeling of an aluminum billet extrusion: (a) initial configuration, the deformed meshes at (b) 25%, (c) 50%, (d) 75% and (e) 100%.

$$\frac{\partial L}{\partial \varepsilon_v^p} = \frac{1}{D(W-\varepsilon_v^p)} \frac{1}{1+R\theta+R\beta\gamma e^{-\beta L}}, \tag{33}$$

$$\frac{\partial b}{\partial \varepsilon_v^p} = \frac{1}{R}\left(\frac{\partial X}{\partial \varepsilon_v^p} - \frac{\partial L}{\partial \varepsilon_v^p}\right). \tag{34}$$

4.2. Model assessment

In order to evaluate the parameters of double-surface plasticity, it is necessary to obtain these values for the fixed, moving cap and tension cut-off yield surfaces. The fixed yield surface has an exponential form which is composed of an initial portion of the Drucker–Prager envelope joined smoothly to the subsequent Drucker–Prager line, as demonstrated in Fig. 3(a). The slope of the first Drucker–Prager line, i.e. line I, is grater than the slope of the second Drucker–Prager line, i.e. line II. The logic for adopting the second Drucker–Prager surface in higher stresses is based on the observation that at higher stresses the material behaves like a liquid. This was adopted particularly to simulate behavior of cohesionless materials subjected to high stresses.

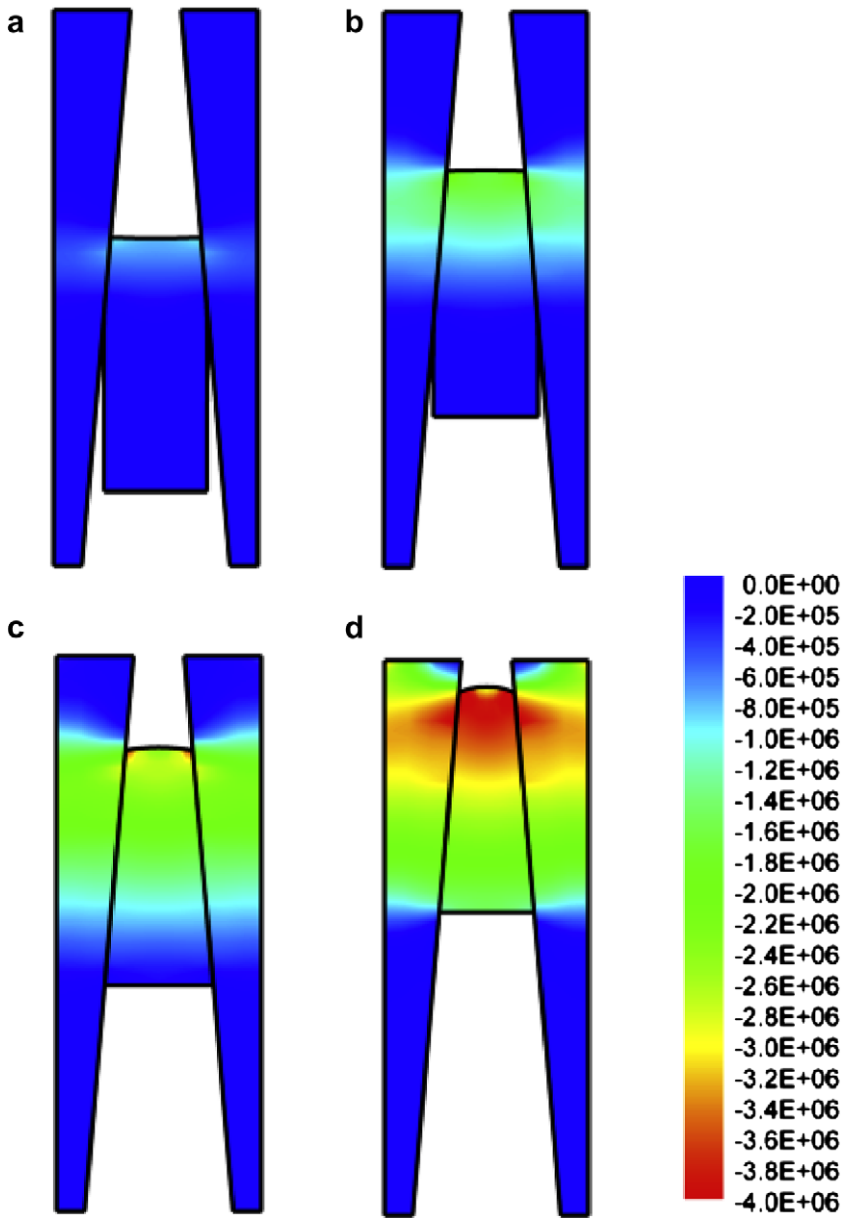

Fig. 12. The radial stresses contours of an aluminum billet extrusion at: (a) 25%, (b) 50%, (c) 75% and (d) 100%.

In order to determine the parameters of fixed yield surface f_1, the results of triaxial tests are necessary at the ultimate shear stresses. These ultimate points are presented in Fig. 3(b) in $J_1 - \sqrt{J_{2D}}$ plane. Considering the state of stress when J_1 is equal to zero and substituting $J_1 = 0$ in Eq. (24) lead to

$$f_1 = \sqrt{J_{2D}} + \gamma - \alpha = 0. \tag{35}$$

It means that the intersection of the fixed yield surface, or the Drucker–Prager line I, with $\sqrt{J_{2D}}-$ axis is α–γ. As β is assumed to be a positive quantity and compression is taken as positive, the quantity of $e^{-\beta J_1}$ will be very small for large value of J_1. Thus, it leads to

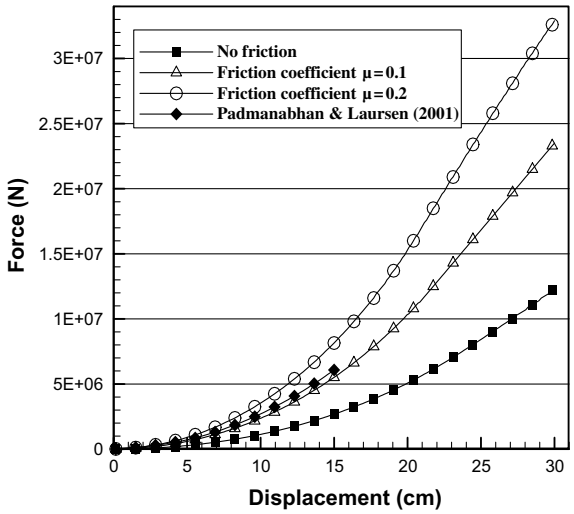

Fig. 13. The variations of vertical force with displacement for an aluminum billet extrusion.

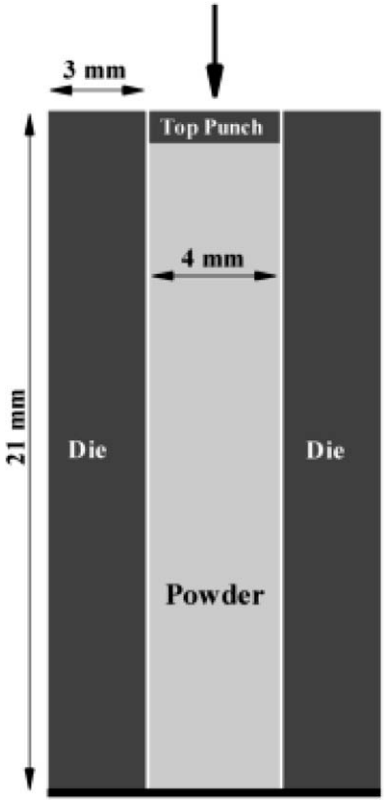

Fig. 14. A plain bush component; the geometry and boundary conditions.

$$f_1 = \sqrt{J_{2D}} - \theta J_1 - \alpha = 0. \tag{36}$$

The above equation represents the Drucker–Prager yield criterion, which is shown by line II in Fig. 3. As can be observed the slope of this line is θ and its intersection with $\sqrt{J_{2D}}$-axis is α. The parameter β in fixed yield surface can be evaluated using an arbitrary point on transition curve, as shown in Fig. 3(b).

In order to determine the parameters of moving cap surface f_2, we need to investigate the plastic deformations under compression. The increase of compression causes the increase of plastic volumetric strain and hence, the expansion of cap surface in J_1-axis. The values of D, W and X_0 can be computed by using Eq. (27). The value of X_0 is zero when there is no significant initial yielding cap. For granular and porous materials, there is no significant initial stress and $X_0 = 0$. The values of D and W can be obtained from the confining pressure, or hydrostatic pressure test. From these tests, the value of X obtained by relation (27) is equal to J_1. The elastic volumetric strain ε_v^e can be evaluated from the variation of J_1 with ε_v on unloading portion curve obtained from the hydrostatic pressure test. The plastic volumetric strains ε_v^p can be expressed in terms of total and elastic components of strain, i.e. $\varepsilon_v^p = \varepsilon_v - \varepsilon_v^e$. The values of D and W can be estimated using the variation of J_1 and X with ε_v^p. The parameter R can be determined using the confining pressure and a set of triaxial tests. For the cap yield surface with a given value of X, the shape of surface can be specified in $J_1 - \sqrt{J_{2D}}$ plane for the same values of plastic

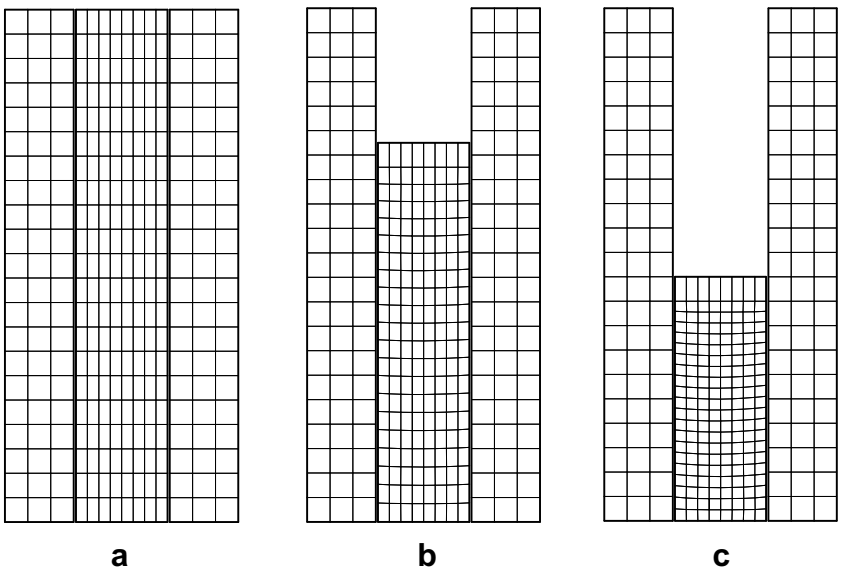

Fig. 15. Finite element modeling of a plain bush component: (a) initial configuration, (b) deformed mesh at 50% and (c) deformed mesh at 100%.

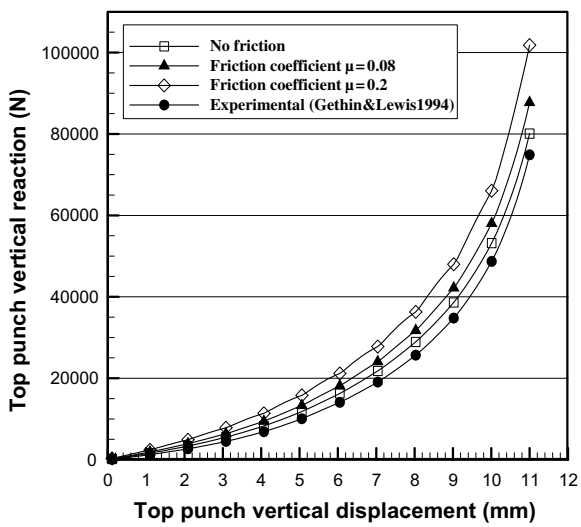

Fig. 16. A plain bush component: the variations of top punch force with displacement at different friction coefficients.

volumetric strain from different hydrostatic and triaxial tests. Fig. 4 shows how the cap yield surface grows with densification due to increase of the volumetric plastic strain.

4.3. Parameter determination

In order to illustrate the calibration of material parameters in the constitutive model, a sample of metal powder is simulated by fitting the model to reproduce data from isostatic compaction and triaxial compression tests. The experimental data are gained from a set of compaction experiments on an iron-based powder (95% by weight) performed by Doremus et al. (1995). Both isostatic compaction and triaxial tests are driven. The raw material is composed of iron, copper, wax and zinc stearate, in which the last two components are admixed as internal lubricants. The density of the solid phase is about 7.54 g/cm^3 and the tap powder density is about 3.67 g/cm^3. The particles have irregular shapes and their sizes are between 10 and 100 μm.

The compacted specimen has an initial height of 42 cm and diameter of 20 cm. The triaxial tests consist of an initial isostatic compaction step up to pressure value of 400 MPa, followed by a subsequent uniaxial compaction step. This step is carried out by keeping pressure constant and increasing the axial stress up to the maximum value of 1250 MPa. The material model parameters of iron powder for the double-surface cap plasticity are given in Table 1. The initial relative density is

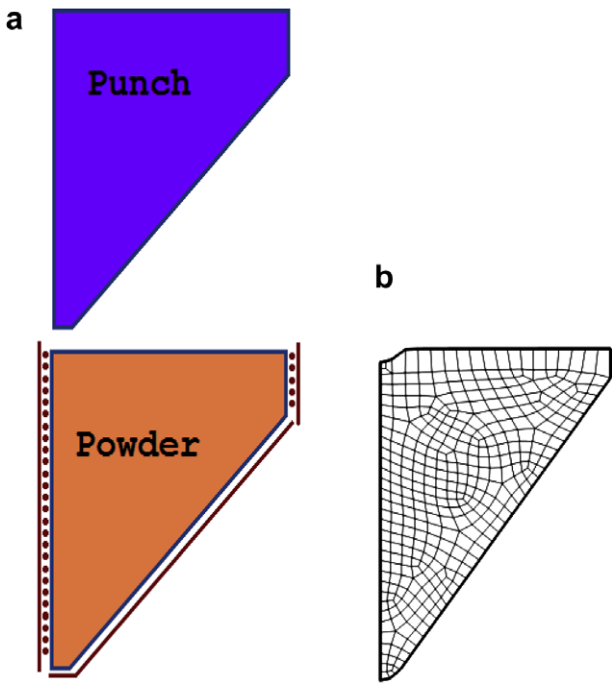

Fig. 17. A shaped-charge liner: (a) geometry and (b) initial FE mesh.

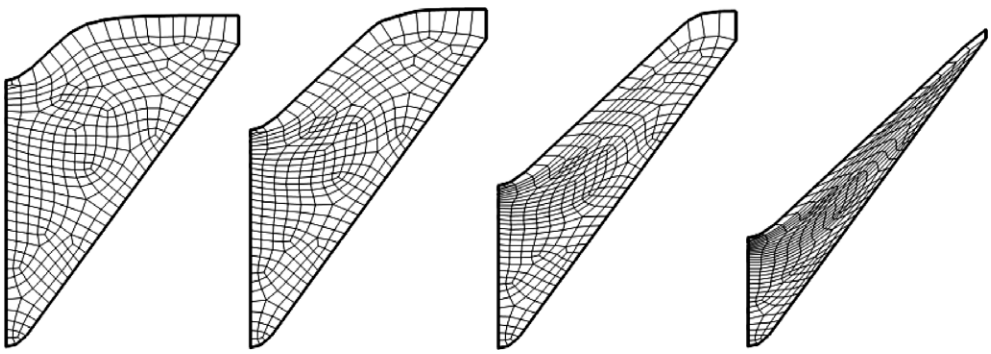

Fig. 18. A shaped-charge liner: the deformed meshes.

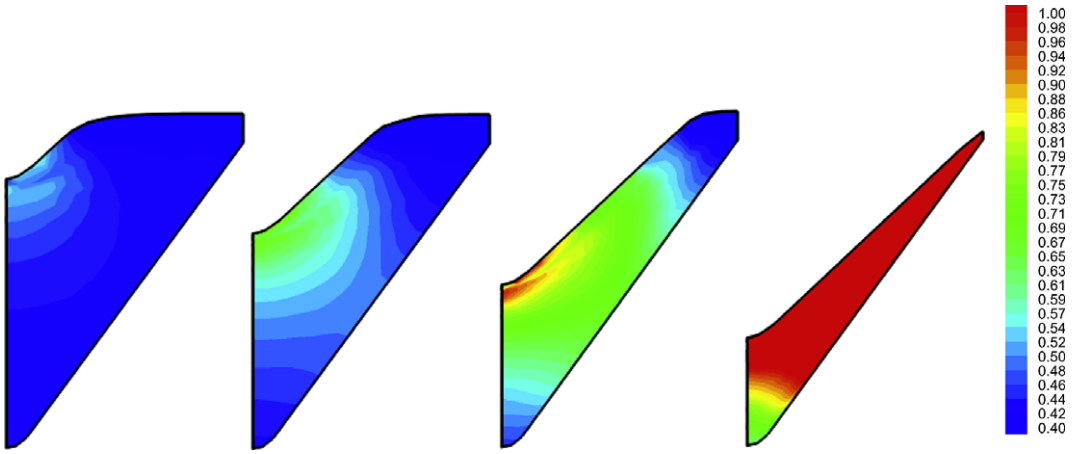

Fig. 19. A shaped-charge liner: the distribution of relative density contours at different compaction processes.

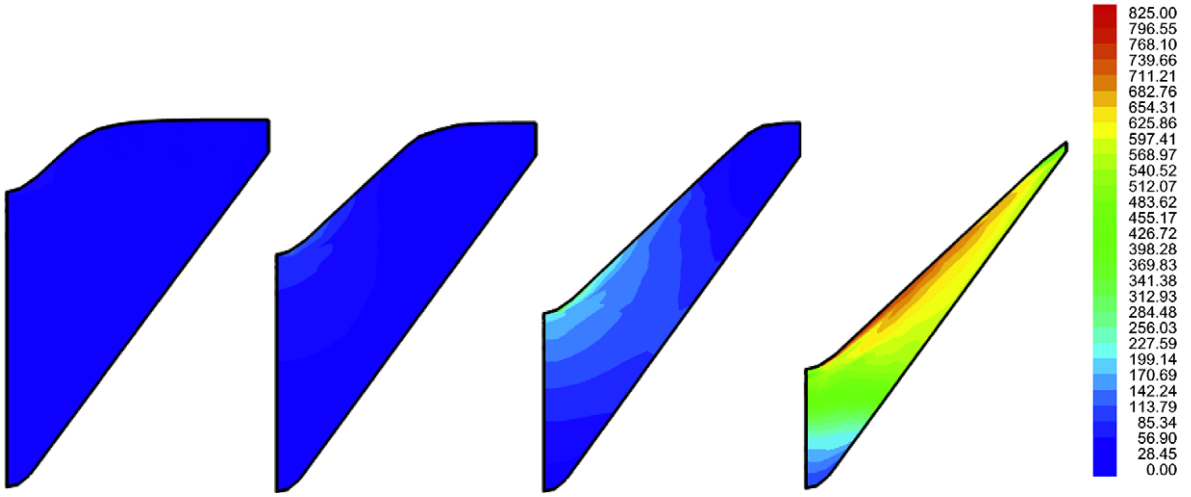

Fig. 20. A shaped-charge liner: the distribution of normal stress σ_y (MPa) contours at different compaction process.

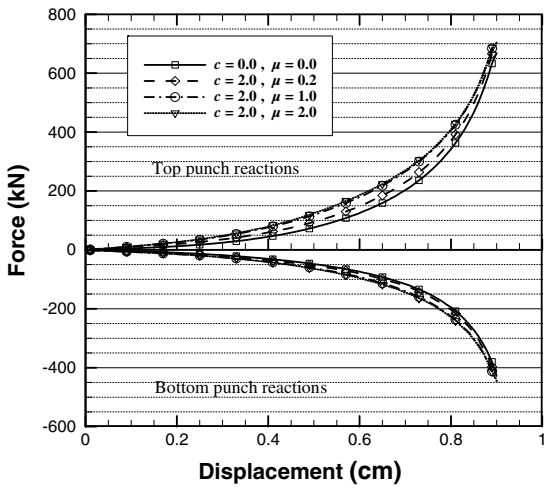

Fig. 21. The variations of the punch forces with displacement at different cohesion and friction coefficients.

$\bar{\rho}_0 = 0.4$ and the Poisson's ratio is $\nu = 0.3$. The variation of the Young modulus with relative density for iron powder is assumed as $E = 3640\bar{\rho}^{3.9}$ (MPa), with $\bar{\rho}$ denoting the relative density (Khoei, 2002).

Fig. 5(a) presents the evolution of the density versus the hydrostatic pressure. This evolution is the characteristic of metal powders. The experimental and numerical results are compared for the isostatic compression step. The applicability of the proposed cap plasticity to handle the volumetric terms is evident in this figure. Fig. 5(b) corresponds to the complete triaxial compression tests. The density versus axial strain curves are plotted for different values of the hydrostatic pressure attained at the end of isostatic compression step. Remarkable agreements between experimental and numerical results are obtained.

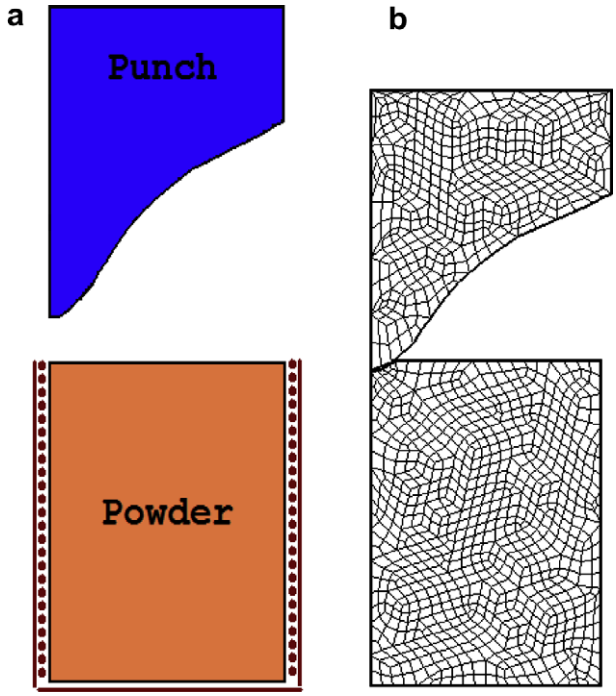

Fig. 22. Piercing problem: (a) geometry and (b) initial FE mesh.

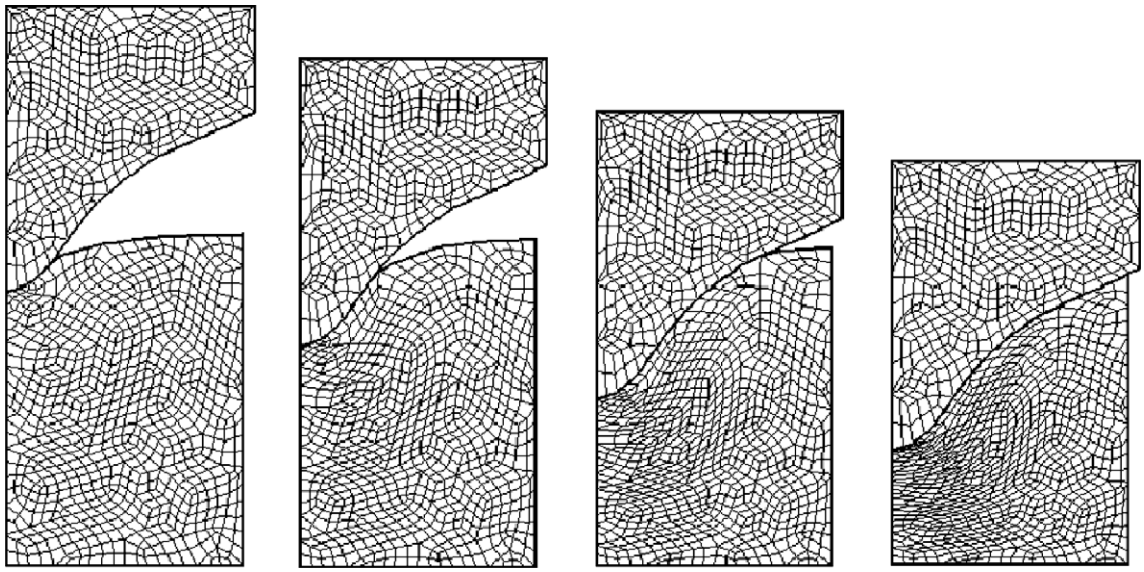

Fig. 23. Piercing problem: the deformed meshes.

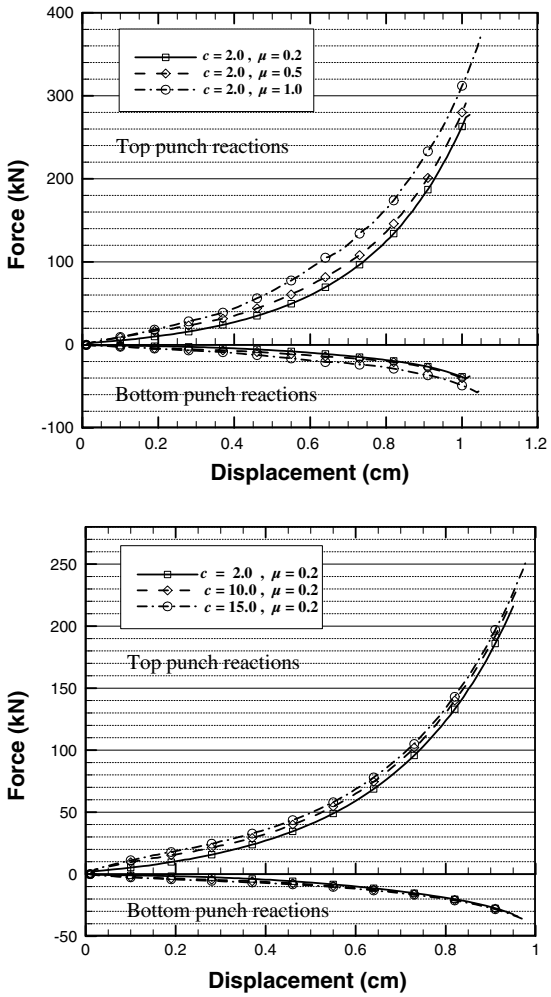

Fig. 24. The variations of the top and bottom punch forces with displacement for various contact conditions.

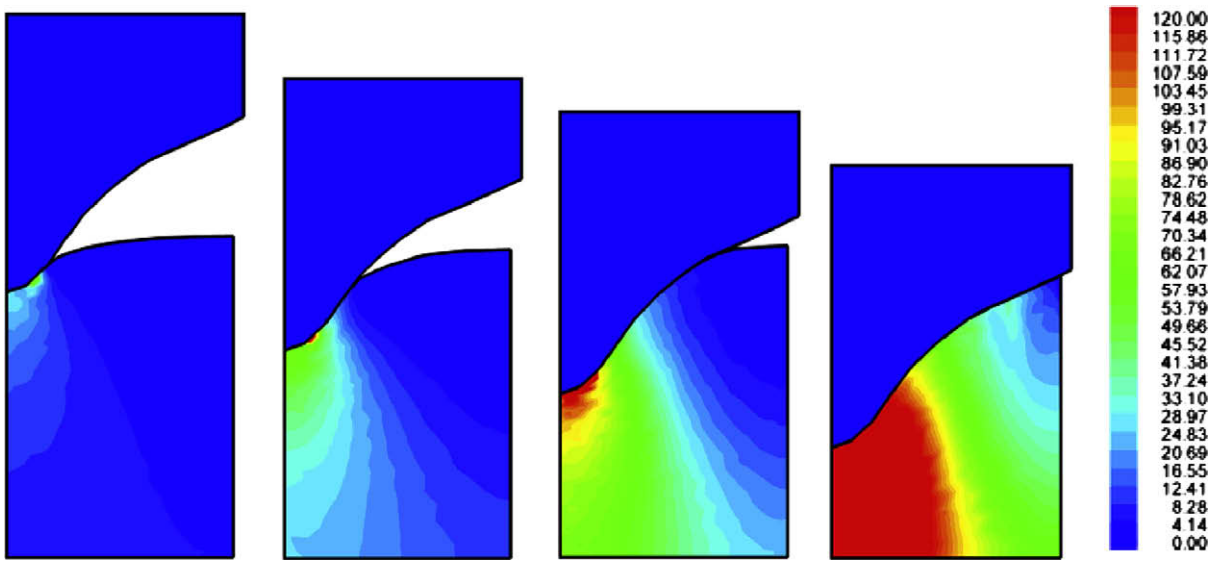

Fig. 25. Piercing problem: the distribution of normal stress σ_y (MPa) contours at different compaction processes.

5. Numerical simulation results

In order to illustrate the applicability of the proposed contact friction model together with the large FE deformation and powder constitutive model presented in preceding sections, the powder behavior during the compaction process of a set of powder components are analyzed numerically. The frictional contact algorithm, the elasto-plasticity constitutive matrix of powder, and the large deformation formulation, presented in Sections 2–4, have been implemented in a nonlinear finite element code to evaluate the capability of the model in simulating powder compaction process.

The first two examples, i.e. the plane strain stretching of a thin sheet by a cylindrical punch and the extrusion of an aluminum billet are chosen to demonstrate the efficiency and accuracy of computational algorithm. Due to significant changes in geometry of components, the capability of proposed technique for handling the large deformation under frictional contact behavior is verified. The next four simulations are chosen to demonstrate the efficiency and accuracy of computational algorithm in the modeling of a set of die-powder pressing, including: a plane bush component, a shaped-charge liner, the piercing problem and spike forming. All numerical examples have been solved under displacement control condition by increasing the punch movement and predicting the compaction forces at different displacements. The distribution of stress and relative density contours are presented at different stages of compaction. In the FE simulations, the tools are modeled as rigid bodies, because the elastic deformation of the tools has only an insignificant influence on the density distribution in the green component.

5.1. Stretching of a thin sheet by a cylindrical punch

The first example is of a plane strain stretching of a thin sheet by a cylindrical punch. This problem is typical for thin sheet metal forming applications. The geometry and boundary conditions for this example are shown in Fig. 6. The analysis is performed employing a 2D representation, restricting the deformations to be symmetric along $X_1 = 0$ and imposing the plane-strain boundary condition in X_2-direction. The problem is solved for the final deformed configuration of punch displacement $D_p = 0.25L$ and friction coefficient of $\mu = 0.3$. The convergence tolerance is set to 10^{-5} and the total number of 12 increments is applied.

Fig. 7 presents the finite element model at initial configuration together with the deformed meshes at 50% and final configuration of pressing. The distribution of stress contours in X_1-direction is shown in Fig. 8 at the half and final stages of pressing. This figure clearly presents an appropriate distribution of stresses obtained by imposing the contact constraints at the contact surface of component and punch. Finally, the diagram of punch reaction force versus vertical displacement is presented in Fig. 9, which can be compared with those reported by Peric and Owen (1992) using the 3D numerical simulation with different punch set up.

5.2. Extrusion of an aluminum billet

The second example is of the extrusion of an aluminum billet, which is applicable typically in metallurgy engineering. This example illustrates the capability of the proposed node-to-surface technique, which can be particularly useful in

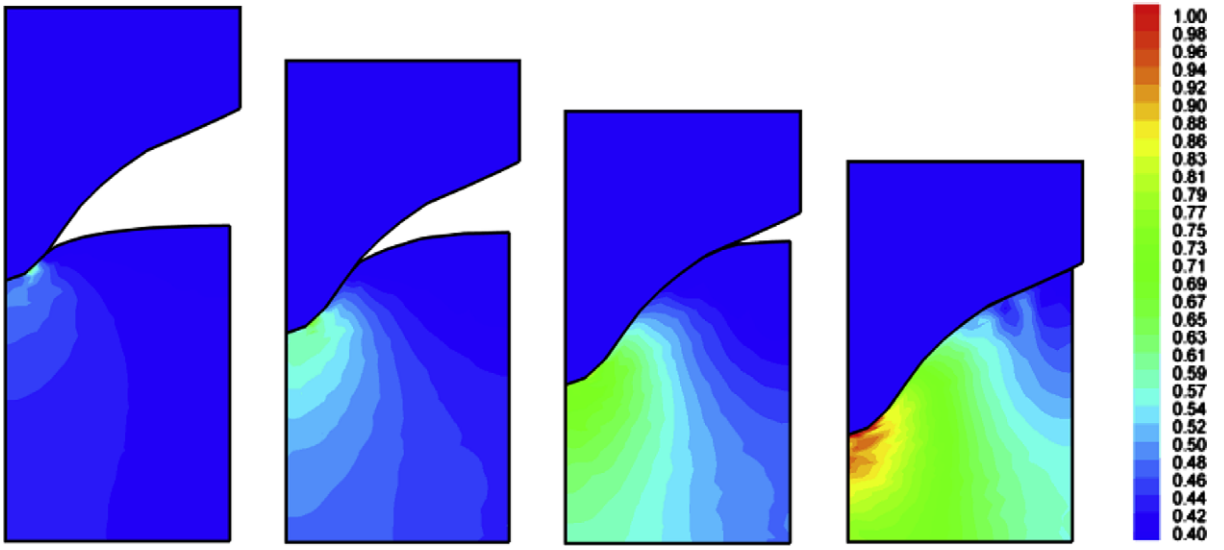

Fig. 26. Piercing problem: the distribution of relative density contours at different compaction processes.

modeling of contact constraints. Two bodies with frictional surfaces are in contact, large deformations are expected, and considerable geometrical nonlinearity behavior is included in the mechanical description. The smoothed and non-smoothed frictional contact conditions were proposed by Padmanabhan and Laursen (2001) for this example, and is available for comparison. Several geometrical complications are included in this problem by inclining the master surface. An efficient search algorithm is used for each slave node, which can be easily determined by the relative master segment at different angle of master segments. The bottom nodes of the billet are subjected to a uniform upward displacement and the outer boundaries of the die are considered fixed. The material properties of the billet are chosen as; $K = 63.84$ GPa and $G = 26.12$ GPa. The material properties of the die are chosen so that to ensure significant deformation on both sides of the contact surface; $K = 0.6384$ GPa and $G = 0.2612$ GPa. The Coulomb frictional contact law is used with the friction coefficient of $\mu = 0.2$.

In the present simulation, the billet is forced to move upward with the total movement of 300 mm by using an incremental displacement control approach. The initial geometry and boundary conditions are shown in Fig. 10. The finite element

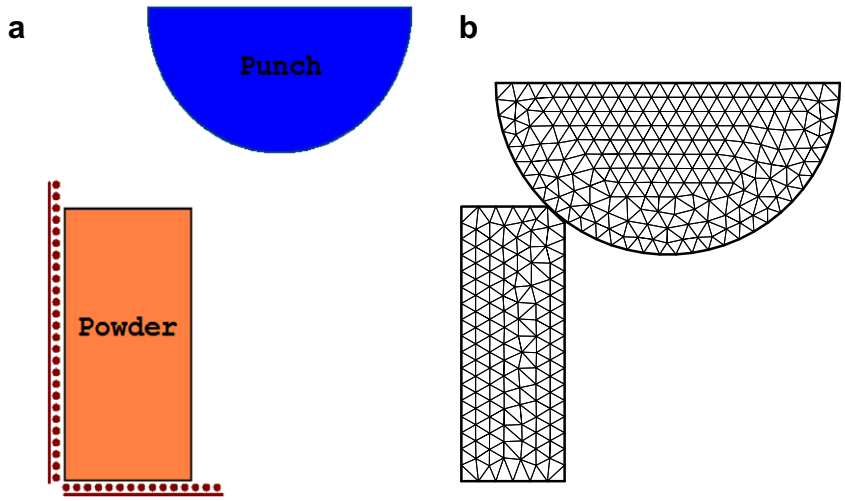

Fig. 27. Spike forming: (a) geometry and (b) initial FE mesh.

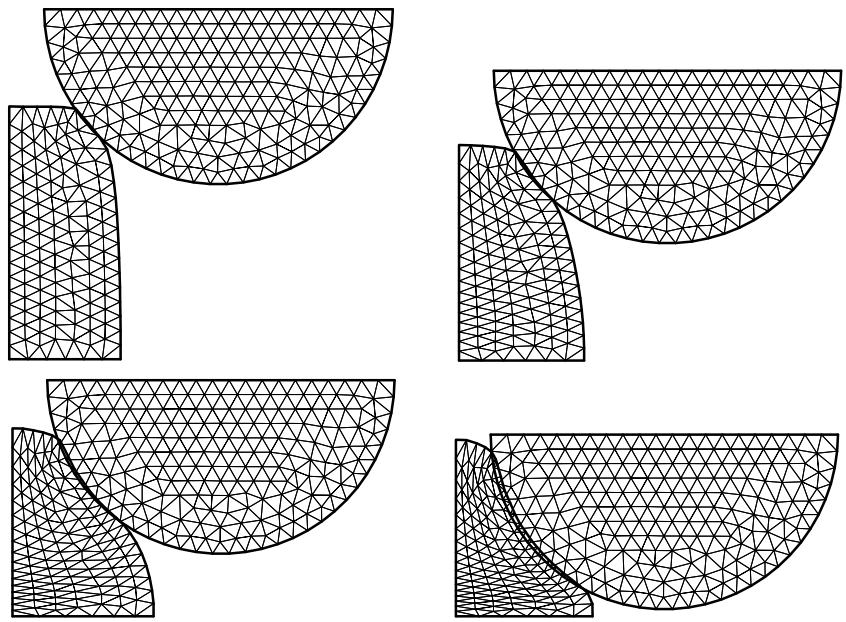

Fig. 28. Spike forming: the deformed meshes.

model at the initial configuration together with the deformed meshes at 25%, 50%, 75% and final configuration of process are depicted in Fig. 11. In Fig. 12, the distribution of radial stress contours are shown at different stages of process. The results are in complete agreement with those reported by Padmanabhan and Laursen (2001). Clearly, the maximum compressive stress happens at the top region of the billet where the contact occurs. In Fig. 13, the variations of vertical force with displacement are shown at different friction coefficients. As can be seen, the force-displacement curve of friction coefficient $\mu = 0.1$ is identical with that obtained by Padmanabhan and Laursen (2001).

5.3. A plain bush component

In third example, the uniaxial compaction of a plain bush component, which is extensively used in mechanical engineering, is modeled numerically. This example is chosen to demonstrate the performance and accuracy of proposed computational algorithm for simulation of the frictional contact constraint in powder compaction process. The experimental data reported by Gethin and Lewis (1994) is available for this example and is used for comparison. A cylindrical component of powder with the inner and outer radiuses of 8.5 and 12.5 mm and initial length of 20.0 mm has been solved with displacement control by increasing the top punch displacement up to 11 mm while bottom punch is fixed. The direction of displacement is always in a vertical direction which represents the axial punch load. The component is made from a mixture of different metallic powders with the material parameters of double-surface plasticity given in Table 1. The die wall friction simulated with the Coulomb friction coefficients of $\mu = 0.08$, 0.1 and 0.3.

The geometry configuration and boundary condition are depicted in Fig. 14. The finite element modeling of bush component is performed using an axi-symmetric model. The FE model of plain bush at the initial configuration together with the deformed meshes at the half and final stages of compaction are depicted in Fig. 15. Clearly, it can be seen from the analysis that the flow pattern is a consequence of two distinct effects. First, the single punch motion gives maximum powder movement at the top punch and reduces to zero movement at the bottom punch. Secondly, the effect of friction causes different powder movement through the radius of the bush. Finally, the variations of the top and bottom punch forces with displacement are plotted in Fig. 16 at different friction coefficients. The result is in good agreement with that reported experimentally by Gethin and Lewis (1994) at $\mu = 0.08$.

5.4. A shaped-charge liner

The next example is of a shaped-charge liner, which is extensively used for civilian oil and steel sectors in geophysical prospecting, mining, and quarrying. Most liners used in the civilian sector are often made from a mixture of different metallic powders. This component has been simulated by Gu et al. (2001) using different punch set up. In the present simulation, a shaped-liner is pressed from the iron powder with the material parameters given in Table 1. The schematic of the process to form a shaped-charge liner from iron powder along with the geometry and initial FE mesh of powder before compaction are

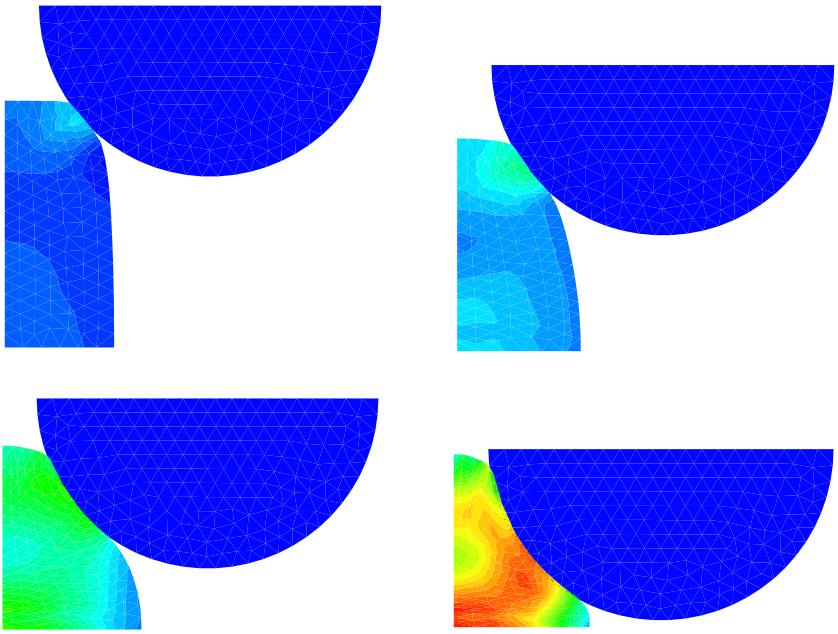

Fig. 29. Piercing problem: the distribution of relative density contours at different compaction process.

presented in Fig. 17. The loading characteristics are achieved by the use of prescribed nodal displacements for the top punch movement. The die and upper punch are modeled as rigid surfaces. The simulation has been performed using the remaining pressing distance of 9.0 mm from above. In Fig. 18, the deformed finite element meshes of the component are presented at four different stages of compaction.

In Fig. 19, the predicted relative density distributions are shown at different stages of compaction for $c = 2.0$ MPa and $\mu = 0.2$. At the end of the compaction, the relative density contour show that the compaction occurs almost uniform in the component and the only low region of density appears at the bottom-left corner, which increases gradually to the top and right-hand side of component. In Fig. 20, the results of normal stress σ_y contours are shown at different stages of compaction. It is clear from the figure that the effects of cohesion and wall friction cause the lower values of stress at two regions; the bottom-left corner and the top-right corner, which can cause a crack or a reduction of the ultimate strength of the finished compacted component. Finally, the variations of the top and bottom punch forces with displacement are plotted in Fig. 21 for different values of cohesion and friction coefficient. This figure clearly shows the effect of cohesion and friction coefficient on the punch reactions.

5.5. Piercing problem

In next example, a workpiece which is compacted from iron powder with a mechanical press and a multi-platen die set is simulated numerically using the proposed computational algorithm. The shape of powder together with the die and punch in their position before compaction are presented in Fig. 22. Also plotted in this figure is the initial FE mesh of uncompacted powder and the punch. The compaction is employed by the action of top punch movement, as shown in Fig. 22. The simulation has been performed using the remaining pressing distance of top punch of 10.5 mm. The die wall friction is simulated with the Coulomb friction coefficients $\mu = 0.2$, 5.0 and 10.0, and cohesions $c = 2.0$, 10.0 and 15.0 MPa. In Fig. 23, the deformed FE meshes of the component are presented at four different stages of compaction. The present numerical simulation clearly shows how the gap between the powder and punch decreases and the effect of frictional contact is incorporated into account during the process of compaction.

In Fig. 24, the variations of the top and bottom punch forces are plotted with displacement for various contact conditions. The results of normal stress σ_y contours are shown in Fig. 25 at different stages of compaction for $c = 2.0$ MPa and $\mu = 0.2$. At the end of the compaction, the contour of normal stress shows the highest stress values at the left part of component, which reduces gradually to the right-hand side. In Fig. 26, the predicted relative density distributions are presented at different stages of compaction. The contour of final relative density illustrates the highest values of density at the left bottom-corner of punch surface, and the lowest values of density at the right-hand side, where the lowest values of stresses are obtained.

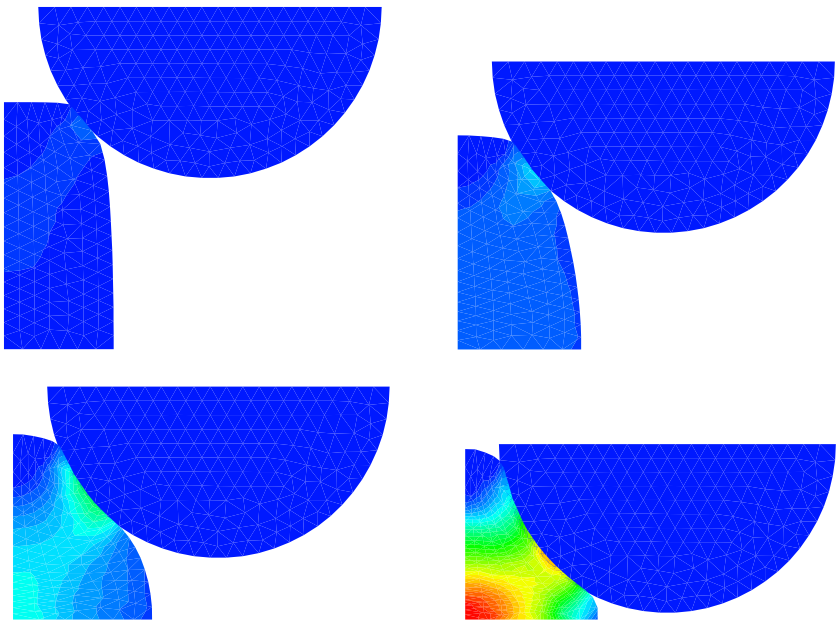

Fig. 30. Piercing problem: the distribution of normal stress σ_y (MPa) contours at different compaction processes.

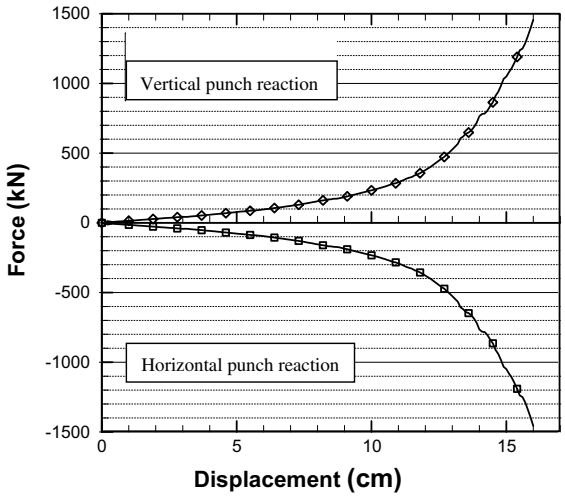

Fig. 31. The variations of the vertical and horizontal punch forces with displacement for piercing problem.

5.6. Spike forming

The last example demonstrates the performance of present formulation in complicated die geometry and simultaneous high distortional and volumetric deformation of elements. In the production of this component the compaction starts from loose powder by moving the upper punch downward to its final position 16 mm, while the bottom punch is fixed. The schematic of the process to form an industrial component along with the geometry and FE meshes of powder and punch before compaction are presented in Fig. 27. The loading characteristics are achieved by the use of prescribed nodal displacements for the top punch movement. The die and upper punch are modeled as rigid surfaces. The contact friction is simulated using $c = 2.0$ MPa and $\mu = 0.2$.

In Fig. 28, the deformed FE meshes of the component are presented at four top punch movements. In Figs. 29 and 30, the development of the normal stress σ_y and the distributions of relative density of powder are investigated in the compressed component at various stages of compaction. At the end of the compaction, the contours display the lowest values of stress and density at two regions; the top corner and the bottom right-hand side, which increases gradually to the middle part of component. Finally, the variations of the top punch forces in x- and y-directions are plotted with displacement in Fig. 31 for the Coulomb friction coefficient $\mu = 0.2$ and cohesion $c = 2.0$ MPa. This example clearly presents the capability of proposed computational algorithm in modeling contact friction for large plastic deformation of powder compaction processes.

6. Conclusion

In the present paper, the influence of powder-tool friction was presented in large deformation simulation of powder forming processes. The numerical modeling of frictional contact between a rigid tool and a deformable material was performed by the use of a new computational algorithm in the concept of the penalty approach based on the node-to-surface algorithm. The frictional properties on the contact surface were performed using a simple and efficient method. A plasticity theory of friction based on a Coulomb friction law was incorporated to simulate sliding resistance at the powder-tool interface. The frictional contact formulation was performed within the framework of large FE deformation in order to predict the non-uniform relative density distribution during large deformation of powder die pressing. A double-surface cap plasticity model was employed for description of powder behavior.

Finally, the capability and efficiency of the proposed contact friction model together with the large FE deformation and powder constitutive model was presented in numerical modeling of a set of forming processes, including: a plane strain stretching of a thin sheet by a cylindrical punch, the extrusion of an aluminum billet, the compaction process of a plain bush component, a shaped-charge liner, the piercing problem and the spike forming. The distribution of stress and relative density contours are presented at different stages of compaction. The results of various contact conditions clearly present the effect of cohesion and friction coefficient at the powder-tooling interface on the punch reaction. The comparisons were performed with experimental and numerical results reported in literature. The numerical simulation results indicated that the proposed computational algorithm makes it possible to simulate the complex phenomena of frictional contact in the powder forming problems efficiently and accurately.

References

Aydin, I., Briscoe, B.J., Sanliturk, K.Y., 1996. The internal form of compacted ceramic components. A comparison of a finite element modeling with experiment. Powder Technology 89, 239–254.

Beer, G., 1985. An isoparametric joint/interface element for finite element analysis. International Journal for Numerical Methods in Engineering 21, 585–600.
Belyschko, T., Neal, M.O., 1991. Contact-impact by the pinball algorithm with penalty and Lagrangian methods. International Journal for Numerical Methods in Engineering 31, 547–572.
Benson, D.J., Hallquist, J.O., 1990. A single surface contact algorithm for the post-buckling analysis of shell structures. Computers Methods in Applied Mechanics and Engineering 78, 141–163.
Brandt, J., Nilsson, L., 1999. A constitutive model for compaction of granular media, with account for deformation induced anisotropy. Mechanics of Cohesive Frictional Materials 4, 391–418.
Brekelmans, W.A.M., Janssen, J.D., Van de Ven, A.A.F., de With, G., 1991. An Eulerian approach for die compaction processes. International Journal for Numerical Methods in Engineering 31, 509–524.
Cameron, I.M., Gethin, D.T., 2001. Exploration of die wall friction for powder compaction using a discrete finite element modeling technique. Modeling and Simulation in Materials Science and Engineering 9, 289–307.
Chaudaray, A.B., Bathe, K.J., 1986. A solution method for static and dynamic analysis of contact problems with friction. Computer and Structures 24, 855–873.
Curnier, A., Alart, P., 1988. Generalisation of Newton type methods to contact problems with friction. Journal de Mecanique Theorique et Appliquee 7, 67–82.
Doremus, P., Geindreau, C., Martin, A., Debove, L., Lecot, R., Dao, M., 1995. High pressure triaxial cell for metal powder. Powder Metallurgy 38, 284–287.
Ernst, E., Thummler, F., Beiss, P., Arnhold, V., 1991. Friction measurements during powder compaction. Powder Metallurgy International 22, 77–84.
Fleck, N.A., 1995. On the cold compaction of powders. Journal of Mechanics and Physics of Solids 43, 1409–1431.
Gethin, D.T., Lewis, R.W., 1994. Finite element modeling of powder compaction and its experimental validation. Powder Metallurgy World Congress, Paris, 689–692.
Giannakopoulos, A.E., 1989. The return mapping method for the integration of friction constitutive relations. Computers and Structures 32, 157–167.
Gu, C., Kim, M., Anand, L., 2001. Constitutive equations for metal powders: application to powder forming processes. International Journal of Plasticity 17, 147–209.
Haggblad, H.A., Oldenburg, M., 1994. Modeling and simulation of metal powder die pressing with use of explicit time integration. Modeling and Simulation in Materials Science and Engineering 2, 893–911.
Khoei, A.R., 2002. Numerical simulation of powder compaction processes using an inelastic finite element analysis. Materials and Design 23, 523–529.
Khoei, A.R., 2005. Computational Plasticity in Powder Forming Processes. Elsevier, Amsterdam.
Khoei, A.R., Azami, A.R., 2005. A single cone-cap plasticity with an isotropic hardening rule for powder materials. International Journal of Mechanical Sciences 47, 94–109.
Khoei, A.R., Azami, A.R., Anahid, M., Lewis, R.W., 2006. A three-invariant hardening plasticity for numerical simulation of powder forming processes via the arbitrary Lagrangian–Eulerian FE model. International Journal for Numerical Methods in Engineering 66, 843–877.
Khoei, A.R., Bakhshiani, A., 2004. A hypoelasto-plastic finite strain simulation of powder compaction processes with density dependent endochronic model. International Journal of Solids and Structures 41, 6081–6110.
Khoei, A.R., Bakhshiani, A., Mofid, M., 2003. An endochronic plasticity model for finite strain deformation of powder forming processes. Finite Elements in Analysis and Design 40, 187–211.
Khoei, A.R., Lewis, R.W., 1998. Finite element simulation for dynamic large elasto-plastic deformation in metal powder forming. Finite Elements in Analysis and Design 30, 335–352.
Khoei, A.R., Lewis, R.W., 1999. Adaptive finite element remeshing in a large deformation analysis of metal powder forming. International Journal for Numerical Methods in Engineering 45, 801–820.
Kim, K.T., Lee, H.T., 1998. Effect of friction between powder and mandrel on densification of iron powder during cold isostatic pressing. International Journal of Mechanical Sciences 40, 507–519.
Laursen, T.A., Simo, J.C., 1993. A continuum-based finite element formulation for the implicit solution of multibody, large deformation frictional contact problems. International Journal for Numerical Methods in Engineering 36, 3451–3485.
Laursen, T.A., Simo, J.C., 1993. Algorithmic symmetrization of Coulomb frictional problems using augmented Lagrangians. Computer Methods in Applied Mechanics and Engineering 108, 133–146.
Lewis, R.W., Khoei, A.R., 2001. A plasticity model for metal powder forming processes. International Journal of Plasticity 17, 1659–1692.
Padmanabhan, V., Laursen, T.A., 2001. A framework for development of surface smoothing procedures in large deformation frictional contact analysis. Finite Element in Analysis and Design 37, 173–198.
Peric, D., Owen, D.R.J., 1992. Computational model for 3D contact problems with friction based on the penalty method. International Journal for Numerical Methods in Engineering 35, 1289–1309.
Pietrzak, G., Curnier, A., 1999. Large deformation frictional contact mechanics: continuum formulations and augmented Lagrangian treatment. Computer Methods in Applied Mechanics and Engineering 177, 351–381.
Ransing, R.S., Gethin, D.T., Khoei, A.R., Mosbah, P., Lewis, R.W., 2000. Powder compaction modeling via the discrete and finite element method. Materials and Design 21, 263–269.
Simo, J.C., Wriggers, P., Taylor, R.L., 1985. A perturbed Lagrangian formulation for the finite element solution of contact problems. Computer Methods in Applied Mechanics and Engineering 51, 163–180.
Sinka, I.C., Cunningham, J.C., Zavaliangos, A., 2003. The effect of wall friction in the compaction of pharmaceutical tablets with curved faces: a validation study of the Drucker–Prager cap model. Powder Technology 133, 33–43.
Tabata, T., Masaki, S., Kamata, K., 1980. Determination of the coefficient of friction between metal powder and die wall in compaction. International Journal of Plasticity 21, 773.
Wriggers, P., Simo, J.C., 1985. A note on tangent stiffness for fully nonlinear contact problems. Communications in Applied Numerical Methods 1, 199–203.
Wriggers, P., Vu Van, T., Stein, E., 1990. Finite element formulation of large deformation impact-contact problems with friction. Computers and Structures 37, 319–331.